Complex wire grid antennas: determining the optimal source location using characteristic mode analysis

Tuan Phuong Dang [1]*, Adnan F. Alhaj Hasan [2], Talgat R. Gazizov [3]

[1, 2, 3]Department of Television and Control, Tomsk State University of Control Systems and Radioelectronics, 634050 Tomsk, Russia;

1. dang.p.2213-2023@e.tusur.ru, dangtuanphuong01111998@gmail.com, +79131012347, Tomsk, Russia, 634050 (Corresponding Author)

2. alkhadzh@tusur.ru, +7 996 957-97-63, Tomsk, Russia, 634050

3. talgat.r.gazizov@tusur.ru, +79138260724, Tomsk, Russia, 634050

Abstract: Wide use of radioelectronic systems requires more complex antennas. Determining the location of the excitation source (feed) in a complex antenna structure plays an important role and depends on many factors. Currently, this choice is often made based on the designer experience and requires careful modeling and analysis. One of the popular methods used in such programs is the characteristic mode analysis (CMA). However, previous CMA-based studies that determine the source location often considered the excitation of low-order modes. In this paper, we present an algorithm to determine the optimal source location in a wire grid antenna that excites all modes reasonably well. This algorithm is based on the product of characteristic current and modal significance to obtain the maximum possible current distribution along the antenna wires and radiation field. The proposed algorithm is tested here on the example of dipole and conical spiral structures in the frequency ranges of 0.1–1 GHz and 9–11 GHz, respectively, and verified by the method of moments.

Index Terms: characteristic mode analysis, method of moments, excitation source, wire grid, antennas

1. INTRODUCTION

Wide use of radioelectronic systems requires more complex antennas. The process of analyzing and designing antennas is a perpetual challenge for radioelectronics engineers since it requires a seamless blend of specialized knowledge, practical experience, and advanced simulation tools [1, 2]. With the rapid advancement of technology, the demand for high-performance antenna devices and the need to meet increasingly stringent requirements impose new challenges on this field [3, 4]. Designers must consider and optimize a lot of antenna characteristics and parameters, including shape and size, material properties, and radiation field requirements [5, 6].

Although modern antenna simulation software [7] and the extensive design experience accumulated over many years have made antenna analysis and optimization easier, a deep understanding of physical phenomena and the operating principles of antennas remains crucial for breakthrough designs. To address this challenge, characteristic mode analysis (CMA) has emerged as a powerful and effective method that provides designers with profound physical insights leading to significant advancements in antenna design [8, 9]. CMA enables detailed modeling of the distribution of characteristic currents on the surface of a structure, allowing for the prediction of critical antenna characteristics such as surface current distribution and radiation fields [10].

Leveraging these advantages, CMA empowers designers to create and optimize antennas with exceptional performance [11, 12]. Thus, complexity of phenomena during antenna functioning can be described and clarified by characteristic modes.

Among the key factors affecting antenna performance, the source location plays a crucial role. Selecting the optimal source location can significantly influence the magnitude of the radiated field, input impedance, and antenna directivity. However, determining the ideal source location for a specific antenna structure is a complex problem, particularly for modern antenna designs that are increasingly intricate and aim to achieve superior performance [13].

In previous studies, source location determination in CMA-based applications has directly been used, for example, to enhance impedance bandwidth [14–16], design circularly polarized antennas [17], and optimize multiple-input multiple-output (MIMO) systems [18]. For clarity and ease of understanding, in what follows, we briefly summarize these research directions.

Impedance bandwidth enhancement: Observing the frequency dependence of modal significance (MS) in narrowband antennas reveals that modes with high MS values (MS>0.7) are often distributed far apart within a given frequency range. To create a potential wideband operation, the antenna structure or geometry is modified to shift these modes closer together within the same frequency band, ensuring that high-MS modes are positioned in proximity to one another [16]. Then the characteristic currents are analyzed to determine optimal excitation locations, thus ensuring effective activation of the desired modes and achieving the targeted bandwidth.

Designing circularly polarized antennas: Starting from an antenna with linear polarization, modifications in structure and geometry are applied to ensure that two selected modes at frequency *f* satisfy the condition for circular polarization. More specifically, at frequency *f*, the two modes with high, equal MS and 90° phase difference of their characteristic angle [17] must be excited at the locations where their characteristic currents are equal.

MIMO system optimization: In MIMO systems, an alternative to increasing the number of physical antennas is to use multiport antennas. Given that multiple modes exist within a single antenna structure, it is possible to independently excite each mode, forming a multiport antenna where each port activates a distinct mode [18]. This approach significantly improves port isolation, enhances MIMO system performance, and optimizes antenna space utilization without increasing the number of radiating elements.

In addition to the above applications, modes can also be selectively excited to optimize the radiation field of the antenna [19]. According to [20], to excite the desired mode, the source needs to be placed at the location with strong characteristic current. In general, previous studies have mainly focused on the excitation of antennas modes with larger MS. However, in practice, high-order modes (mode with smaller MS) also have a significant influence on the current distribution [21].

The aim of this paper is to develop an algorithm that determins the optimal source location (OSL) that excites all modes reasonably well and maximizes surface current and antenna radiation field over the considered frequency range by analyzing the product of characteristic current and MS using CMA.

Among commonly used antennas, wire grid (WG) antennas stand out since their design reduces wind impact, antenna mass, and fabrication costs, while maintaining effective radiation characteristics [22, 23]. These advantages make WG antennas ideal for modern communication applications. Therefore, in this work we focus on these antennas exemplified by of dipole and conical spiral antennas. The surface current distribution and radiation pattern results obtained using CMA are verified by comparing them with those obtained using conventional MoM with a pulse basis function (PBF).

This paper is organized as follows. Section II details the developed algorithm used to determine the OSL. Section III presents current distribution and radiation pattern results obtained using the developed MATLAB code based on this algorithm at various source locations for different structures. The analysis of the results allowed determining the OSL, thus demonstrating the effectiveness of the proposed algorithm. Section IV summarizes and discusses the results and highlights the points to consider in future studies, followed by conclusions in Section V.

2. OSL ALGORITHM

To analyze antenna or scatterer structures, the MoM is often used to solve electromagnetic integral equations. As a result of this process, the impedance matrix **Z** is obtained. Subsequently, using CMA and ***Z*** based on the theory in [24], N characteristic modes can be derived where N is equal to the number of segments or here the PBF). Each n-th mode of these N modes is characterized by an eigenvalue λ_n, and an eigenvector (characteristic current) I_n with a size of $N\times 1$.

The surface current (I) can be determined using the equation from [10]:

$$I = \sum_{n=1}^{N} \frac{\langle I_n, V \rangle I_n}{1 + j\lambda_n} \quad (1)$$

where V is the excitation vector. This equation demonstrates that there are three main factors that influence the surface current distribution along the structure: the excitation source amplitude and location (position in the zero vector V), I_n, and λ_n. It is known that as λ_n approaches 0, the contribution of this mode to I increases (resonance occurs when λ_n=0). The quantity representing the contribution of I_n to I, is called modal significance (MS_n) and is determined by the equation from [25]:

$$MS_n = \left| \frac{1}{1 + j\lambda_n} \right|. \quad (2)$$

From equation (2), it can be observed that MS_n depends only on λ_n and is independent of V. Furthermore, when the absolute value of λ_n is very large (indicating that the contribution of I_n to I is minimal), MS_n approaches 0. Conversely, when λ_n=0, MS_n approaches 1. This implies that as MS_n approaches 1, the magnitude of the radiated field (for antennas) or scattered field (for scatterers) is maximized. In many cases, MS_n is more convenient to use than λ_n when analyzing the behavior of modes over a range of frequencies.

The radiated or scattered fields are linearly related to the currents, so the field (E) can be calculated using the characteristic field (E_n) as in [10]:

$$E = \sum_{n=1}^{N} \frac{\langle I_n, V \rangle E_n}{1 + j\lambda_n}. \quad (3)$$

Similar to I, equation (3) shows that the far field inversely depends on λ_n, and it is directly proportional to E_n and also depends on the characteristics of the excitation source $<I_n,V>$. The strength of E_n is directly influenced by the I_n. As I_n increases, it induces a correspondingly stronger E.

Experience has shown that even if a mode n has a small MS_n but a large I_n, it can still make a significant contribution to the overall I. Thus, in addition to eigenvalues, it is also crucial to consider the effect of eigenvectors on the surface current. Numerous simulations have revealed that modes with MS>0.1 (corresponding to $|\lambda_n|$<10) make a substantial contribution to I.

Based on the above discussion, the OSL algorithm designed to maximize surface currents using CMA can be summarized in the following steps:

1. Determine the **Z** matrix using MoM [26].
2. Calculate eigenvalues and eigenvectors for each mode using **Z** and CMA as outlined in [24].
3. Track these modes in the considered frequency range as outlined in [27].
4. Calculate MS for each mode in the considered frequency range using equation (2).
5. For each frequency, identify modes with MS_n greater than 0.1.
6. Determine the absolute value of I_n ($|I_n|$) for each mode from Step 5.
7. Multiply $|I_n|$ by MS_n for each mode from Step 5. This multiplication results in a matrix, referred to here as the **Product of Characteristic Current and Modal Significance** ($PCCMS_n$) [$|I_n| \times MS_n$] of $N \times M$ size where M is the number of modes being considered.
8. Sum the row values of the resulting $PCCMS_n$ matrix, which in turn results in a vector of N size.
9. Identify, in this vector, the index of the element with the maximum value. This index indicates the possible position of the OSL.
10. Test the obtained OSL by placing the source at the peak locations of each different mode in the considered frequency range; then, compare the obtained surface current magnitudes.
11. Make the final decision on the OSL selection based on the obtained maximum current magnitudes (this is applicable if MS_n are not equal; otherwise, consider the direction of the desired radiated field when making decision).
12. Special case: for a specific n mode, when MS_n>0.1 and for others it is equal to 0, directly use this mode to determine the OSL based on the characteristic current peak of this mode.

Thus, using the additional steps 5–9 of the proposed algorithm, which utilize eigenvalues and eigenvectors obtained by CMA, we determine the source location that yields the maximum surface current.

3. RESULTS

3.1. OSL algorithm application to a dipole antenna

To test the proposed algorithm and demonstrate its effectiveness, we first considered a dipole antenna with a length (l) of 0.5 m and a radius of 0.0005 m, divided into N=101 segments and directed along the Oz axis. The surface current distribution was analyzed using CMA based on MoM with PBF when the excitation source (1 V) was placed at various locations across the frequency range of 100–1000 MHz. These results were verified by comparing them with those obtained using the conventional MoM with PBF.

We have recently developed a MATLAB code that uses the CMA algorithm based on the MoM with PBF to analyze wire structures. This program can calculate and display the characteristic current dependence on each segment as a 2D graph. This is important in our algorithm as it allows for an accurate analysis of the characteristic current characteristics on the segments. Meanwhile, this feature is not yet implemented in modern software such as FEKO by Altair.

First, the frequency dependences of *MS* over the specified frequency range were obtained using CMA based on MoM with PBF. To verify these results, they were compared with those obtained using CMA based on MoM with triangular basis functions (TBF) in [25] (Figure 1). We can see that the obtained results agree quite well with each other, and only modes 1, 2, and 3 significantly contribute to the current. Therefore, in this study, determining the OSL focuses on these three modes, which represent 2 first resonant frequencies f_1=290 MHz and f_2=580 MHz, respectively.

Additionally, it is observed that at f=520 MHz, the *MS* of modes 1 and 2 are equal, both approximately 0.3. This indicates that at this frequency, modes 1 and 2 contribute equally to the surface current. Furthermore, at around 800 MHz, the *MS* values for modes 1, 2, and 3 are nearly equal (MS_1=0.302, MS_2=0.326, MS_3=0.285), signifying that at these frequencies, these three modes contribute almost equally to the current.

Based on these findings, we analyzed I_n and its impact on I for each of the following frequencies: 290, 520, 580, and 800 MHz. This analysis included determining the modes with the highest impact on I using their MS_n. Then, based on the analysis results and the OSL algorithm, we predicted the optimal source location along the dipole. After that, this prediction was verified by analyzing I and E obtained when the dipole source was placed at various locations.

Next, we examined the location of the excitation source at the resonant frequency of mode 1 (f=290 MHz). As shown in Figure 1, at this frequency, mode 1 has a significantly higher modal significance than all other modes (MS_1=1, MS_2≈0, MS_3≈0), indicating that only mode 1 substantially contributes to the surface current. The dependences of $I_{1,\,2,\,3}$ and $|I|$ (when the source is placed at different locations) on the number of segments (x=1,… , N) along the length of the dipole are illustrated in Figure 2. It is evident that I_1 reaches its maximum at the midpoint segment of the dipole (x=51). Therefore, it can be concluded that at f=290 MHz, placing the excitation source at the dipole midpoint will yield the highest surface current magnitude. This conclusion aligns with practical experience, as this position is commonly used to excite a conventional dipole.

The considered source locations were x=51 (peak of I_1), x=22 (peak of I_2), and x=12 (peak of I_3). The results clearly indicate that placing the source in the 12th and 22nd segments results in lower surface current distributions compared to placing it at the 51st segment.

The $E_{1,\,2,\,3}$ and radiation patterns (RPs) in the φ=90° plane (when the source was placed at different positions) of the dipole at f=290 MHz are illustrated in Figure 3. It is evident that at f=290 MHz, only mode 1 had the greatest influence on the field; thus, the shape of the dipole radiation pattern

(RP) had the shape of E_1 regardless of the source position in the dipole. To explain this prediction, from equation (1), it can be seen that the result of the multiplication $<I_n,V>$ and MS_n are real numbers that will affect only the current amplitude and, consequently, the field strength. Therefore, field E in equation (3) can be considered as a linear function of E_n, which has the most significant effect on the E shape, and as a result E has the shape of E_1 in this case. From Figure 3b, it is evident that independently of the source location, the obtained RPs had the same shape of E_1 and only differed by the level (caused by the product $<I_n,V>$, since MS_n were equal for various source locations). At the same time, when the source was placed at x=51, the RP results were larger than those when the source was placed at other positions. This difference is true for the logic that the larger the current, the stronger the field.

Next, we determined the OSL at f=520 MHz. As observed in Figure 1, MS_1=MS_2=0.3, while MS_3=0.005, which is significantly smaller than MS_1. Therefore, only I_1 and I_2 need to be considered when determining the source location. Figure 4 illustrates the dependences of $I_{1,\,2,\,3}$ and $|I|$ on x along the dipole length. From Figure 4a, several observations can be made. If the source is placed at the midpoint of the dipole (the 51st segment), only mode 1 will contribute to the total current, as contribution from mode 2 will be 0 due to the symmetry of I_2 around the axis along the dipole. Consequently, it is necessary to select a location other than the midpoint of the dipole for the source placement to ensure contributions from both modes.

From Figure 4a and by applying the proposed algorithm, we determined that placing the source in the 28th segment of the dipole yields the largest surface current. The surface currents were compared when the source was positioned in the 28th, 24th (peak of I_2), and 51st (peak of I_1) segment, as shown in Figure 4b. The results indicate that the surface currents for the 24th and 28th segments are approximately equal in magnitude. This equality is expected since these segments are close to each other, resulting in a similar impact on the surface current. Note that the currents for the 24th and 28th segments are significantly larger than the current for the midpoint location (51st segment). This comparison confirms that the prediction made by the proposed algorithm is indeed reasonable.

The $E_{1,\,2,\,3}$ and RPs of the dipole at f=520 MHz are illustrated in Figure 5. As mentioned above, at f=520 MHz, both mode 1 and mode 2 affected the surface current; therefore, the shape of the field depended on both E_1, E_2 and the source location (in the case where several modes influence the field). Since the RP upper lobes of mode 2 were directed at ±50°, while the RP lobes of mode 1 were directed at 90°, E was directed in the 50–90° range despite of the source location (i.e., it was not possible to change the source location to obtain a field directed outside this range).

From Figure 5b, it can be seen that at θ=1–80°, when the source was placed at x=24 and 28, the RP levels were larger than those at x=51. However, in the range of θ=80–90°, when the source was at x=51, the RP levels were larger than those at x=24 and 28 (since mode 1 had the most significant influence at the dipole center). From Figure 5b, it can be seen that the RP levels of both the upper (±50°) and lower (±130°) lobes, when the dipole was excited at x=24 and 28, were larger than the RP lobes (±90°) levels when the dipole was excited at x=51. This happened because the surface current magnitudes were much larger than those for x=51, when the source was placed at

x=24 and 28 (Figure 4b). Therefore, the antenna RP direction should be considered when selecting the source location using the OSL algorithm.

At f=520 MHz, when the source was placed at x=51, only mode 1 contributed to the current ($<I_2,V>$=0, and I_3 was not considered since MS_3≈0); thus, E had the same shape as E_1. However, when the source was placed at another position (x≠51), mode 2 was excited; thus, both E_1 and E_2 contributed to the E shape. In such case, it was necessary to consider the impact of each mode on the field. When the source was placed at a position that excited mode 2 more, the resulting field had a shape similar to E_2. For example, when the source was placed at x=24, the RP levels were bigger than those for the other positions and smaller than those when E_2 tends to 0 (at 90°). The direction of the E RP upper lobes, when the source was placed at x=24 and 28, was about θ=±55° (while their direction for E_2 was θ=50°). This is because both mode 1 and mode 2 were excited at the same time; thus, the directions of the E RP lobes deviated slightly towards θ=±90° (main lobes directions of E_1).

Next, we examined the source location at a frequency f=580 MHz, corresponding to the resonant frequency of mode 2. As shown in Figure 1, at f=580 MHz, the modal significance values are MS_1≈0.3, MS_2=1, and MS_3=0.016, with MS_3 being significantly smaller than MS_1, and MS_1 being smaller than MS_2. Therefore, only modes 1 and 2 contribute significantly to the overall surface current. Figure 6a illustrates the dependences of $I_{1,2,3}$ on x along the dipole length, calculated using CMA. By following the proposed algorithm, it was found that placing the source in the 26th segment results in the largest surface current. Additionally, it is observed that in the 25th segment, I_2 reaches its peak, and since MS_2>>MS_1, we can predict that placing the source in the 25th segment would also yield a large surface current. We compared the currents obtained when placing the source in the 51st segment (peak of I_1), 25th (I_2), 13th (I_3), and 26th segment (Figure 6b).

We can see that placing the source in the 25th and 26th segments results in the largest surface currents, as anticipated. When the source is positioned in the 13th segment, a smaller surface current is observed compared to the 25th and 26th segment positions. However, the current for the 13th segment position is still greater than that for the 51st segment position. This can be attributed to the fact that for the 13th segment position, the surface current benefits from contributions from both mode 1 and mode 2. In contrast, for the 51st segment position, mode 2 contributes nothing to the total current, leaving only mode 1 to contribute.

The $E_{1,2,3}$ and E RPs of the dipole at f=580 MHz are illustrated in Figure 7. From Figure 1 it is clear that mode 2 had a much larger MS_n than the other modes; thus, the RP had a shape more similar to E_2. From Figure 7b, we can see that the RP upper lobes maximum levels were 0.62 V/m (for x=13), 0.82 V/m (for x=25 or 26), and 0.17 V/m (for x=51). Since the current magnitudes when the dipole was excited at x=25 or 26 were approximately the same, the E levels in these cases were also the same. When the source was placed at x=13, the current magnitudes were smaller than those for x=25 and 26 cases; thus, the E RP levels for the x=13 case were smaller. These levels, when the source was placed at x=51, were the smallest, except at θ=90°, when they were still the largest. The upper lobes of the E RP were directed in the range of ±(50–90°) thanks to the joint contribution of E_1 and E_2. Moreover, at f=580 MHz, the E RP levels were bigger than those at f=520 MHz, since MS_2 for the former was bigger than that for the latter.

Next, we investigated the source location at f=800 MHz where $MS_1 \approx MS_2 \approx MS_3$, indicating that the effects of modes 1, 2, and 3 on the surface current are nearly identical. Figure 8 shows the dependence of $I_{1,2,3}$ and $|I|$ on x along the dipole length. Applying the proposed algorithm, it was found that the OSL is in the 20th segment. We compared $|I|$ generated when the source was placed in the 20th segment with those obtained when the source was placed in the 51st (peak of I_1 and I_3), the 29th (I_2), and the 15th (I_3) segments (Figure 8b). The 15th and 20th segments positions both yielded the highest currents.

The high current observed for the 15th segment position can be attributed to significant contributions from mode 3, along with additional contributions from modes 1 and 2. For the 51st segment position, a somewhat smaller current is observed due to the absence of mode 2 contribution, with only modes 1 and 3 influencing the current (mode 2 is symmetric about the dipole axis). The 29th segment position shows the smallest current, as mode 2 contributes significantly there, while contributions from modes 1 and 3 are minimal compared to other positions. In such case (MS_n are equal), one should consider the direction of the desired radiated field to make the decision on the OSL.

The $E_{1,2,3}$ and RP levels of the dipole at f=800 MHz are illustrated in Figure 9. At f=800 MHz, the modes had equal MS_n, but since I_3 was the largest, E_3 had a significant effect on E (here, the appearance of 3 lobes) if the source was placed at a position that strongly excited mode 3 (x=15 or 51). When the source was placed at x=51, modes 1 and 3 had their maximum impact on I and consequently on E, which in turn led to the appearance of RP lobe at θ=90° with bigger level than that for other source location cases. When the dipole was excited at x=29, mode 2 had its maximum impact on I and consequently on E; thus, E is predicted to be more similar to E_2 and, therefore, E has only 2 lobes. In addition, it is observed that E_2 and E_3 have lobes with maximum levels in the range of ±(40–50°); thus, the E lobes for most source location cases will probably be in that region (because I_2 and I_3 are both larger than I_1).

As shown in Figure 9b when the source was placed at the middle point of the dipole (x=51), a lobe with a maximum level appeared at θ=90°, and two other lobes appeared at 40 and 140°. When the source was placed at x=15 or 20, a lobe with a maximum level appeared at θ=46°, and two other lobes appeared at 93 and 140°. When the source was placed at x=29, the field was the weakest since the current at x=29 was smallest.

The RP lobes with maximum levels for x=51, 15, and 20 cases were almost equal. However, the width of these lobes for the x=51 case (mode 3 with the highest impact) was narrower than that for x=15 and 20 cases (mode 2 with the highest impact). This is because E_3 has a lobe with a maximum level directed at θ=90° with a narrower width than that of E_2 lobes.

For clarity, Table 1 presents the characteristics of I and E when the source is placed at different positions and at various frequencies.

3.2. OSL algorithm application to a conical spiral antenna

Next, to verify the proposed OSL algorithm on more complex structures than dipole antennas, we considered its application to a conical spiral antenna (CSA). CSAs have uniform input impedance, gain, and circular polarization over a broad frequency range [28]. As the name suggests, CSAs have a cone shape with a wide base gradually narrowing at the top. They are made of an electrical wire wound in a spiral around a cone structure and continuing from the large base to the top. The isometric view of the wired CSA and its MATLAB model are shown in Figure 10. This CSA has the following parameters: the large base radius is 0.005 m, the wire radius is 0.0001 m, the height is 0.0208 m, and the total number of wire segments needed to approximate the antenna structure is 300. The number of segments per loop is evenly distributed, with 36 segments per loop, resulting in approximately 8.3 (300/36) loops required to build the model. In this study, the antenna was considered over the frequency range of 9–11 GHz. In practice, to excite the CSA, the power source is usually placed at the tip of the wire, at the largest loop. Here, a source of 1 V was connected to the first segment.

First, the frequency dependences of MS_n for this CSA were obtained using CMA, as shown in Figure 11. It can be seen that the number of modes affecting the surface current (modes with MS>0.1) varies depending on each frequency. It can be seen that the CSA has resonance frequencies at 9.4 and 10.3 GHz. During the antenna development process, designers often focus on optimizing the antenna at these resonance frequencies. Therefore, in this work, we considered the location of the excitation source around these resonance frequencies. For each frequency, the analysis of I_n and its impact on I was performed. This analysis included determining the modes with the highest impact on I using their MS_n, and calculating their $PCCMS_n$. Then, based on the analysis results and the OSL algorithm, we made a prediction about the optimal source location for the CSA. Finally, we verified this prediction by analyzing I and E obtained when placing the CSA source at various locations.

First, the OSL algorithm was applied to the CSA at its first resonant frequency (f=9.4 GHz). Figure 11 shows that at this frequency, there are 5 modes that greatly affect the surface current (the MS_n for these modes were MS_1=0.93, MS_2=0.54, MS_3=0.24, MS_4=0.16, and MS_5=0.14). We can see that mode 1 had the highest MS_n (approximately 1), followed by mode 2 and mode 3, while modes 4 and 5 had quite small MS_n. Thus, we can say that modes 1, 2, and 3 have the greatest influence on the current.

Figure 12 illustrates the dependences of I_n, $PCCMS_n$, and $|I|$ on x (the number of a segment) along the CSA length and CSA RP at 9.4 GHz. It is clear that since I_1 and MS_1 were larger than I_n of the remaining modes, the obtained $PCCMS_1$ was much larger than $PCCMS_n$ of the other modes. Therefore, at f=9.4 GHz, CSA OSL can be determined just by considering $PCCMS_1$. However, in order to obtain more accurate results, the influence of the remaining modes needs to be considered as well.

Figure 12b shows that although MS_2 was about 2 times larger than MS_3, I_2 was about 2 times smaller than I_3; therefore, their $PCCMS_2$ and $PCCMS_3$ were almost equal (and both much smaller than $PCCMS_1$). Similarly, $MS_{4,5}$ were the smallest (only about 0.16 MS_1); thus, their contribution to surface current was the smallest. An easily seen feature when analyzing I_1, ..., I_5 of the CSA at f=9.4 GHz is that their main peaks were located at segments that were quite close to each other. Therefore, all these modes contributed to the surface current when the source was located at any peak according to their maximum (or near maximum) I_n value in this peak region. This indicates that, unlike in the dipole case, placing the source at the peak of one mode does not exclude contributions from the others.

Based on Figure 12b and by applying the OSL algorithm, it can be predicted that when the source is located at x=129, the obtained surface current is the largest. To verify the correctness of this prediction, the surface current was calculated when the feed was placed at the following locations: x=1 (the actual location of the feed), and at x=10, 30, 55, 80, 103, 129, 164, 202, and 255 (the peak positions of the sum of $PCCMS_{1, 2, 3, 4, 5}$). Figure 12c shows that high current obtained when the source was at x=202 and 103 can be explained by the fact that the sum of their *PCCMSs* was also large (only smaller than that for x=129). In addition, the current for the x=255 and 164 cases was slightly smaller than that for the x=129, 202, and 103 cases, since the sum of $PCCMS_{1, 2, 3, 4, 5}$ was bigger. The current obtained for x=1 was the smallest because the product $<I_n,V>$ was very small when compared with those for the other cases.

Based on Figure 12b, it can be concluded that when the source was placed at x=20, 41, 64, 88, 114, 143, 180, 223 and 300, the obtained sum of $PCCMS_{1, 2, 3, 4, 5}$ was the smallest, and as a result the surface current was the smallest. In addition, the current distribution had a shape similar to the absolute value of I_1 shape (there were 9 peaks; the highest peaks occurred at segments higher than 100) (as shown in Figures 12b, c). As mentioned above, this can be explained by the fact that mode 1 has the greatest impact on the surface current. At the same time, it can be seen that when the source was placed at various positions, the obtained current distribution had peaks at similar positions along the length of the structure, again, because the modes had peaks along the antenna at adjacent segments.

From Figure 12d, E for the x=129 case was the strongest, followed by x=202 and 103 cases, while for x=1 it was the weakest. We can also see that when the source was placed at various locations, the main lobes of the obtained fields had quite similar directions (approximately at θ=0°), which can be explained by the fact that the obtained current had the same shape along the entire antenna structure.

Finally, the OSL algorithm was applied to the CSA at f=10.15 GHz. Figure 13 illustrates the dependences of I_n, $PCCMS_n$, and $|I|$ on x (number of segment) along the CSA length and CSA RP at 10.15 GHz. Figure 11 shows that at this frequency, the modes that affect the surface current (MS>0.1) had the following *MSs*: MS_2=0.94, MS_3=0.53, MS_5=0.26, MS_1=0.22, and MS_6=0.14. From Figure 13a, it can be noticed that, although I_2 was not the largest compared to I_n of the other modes, its $PCCMS_2$ was still the highest thanks to its MS_2 (the highest). Moreover, I_3 had approximately the same amplitude as I_2, but since MS_3 was half of MS_2, $PCCMS_3$ was also about half of $PCCMS_2$. I_5 was slightly larger than I_2 and I_3, but MS_5 was much smaller than MS_2 (by about 3.6 times) and MS_3 (by about 2 times); thus, $PCCMS_5$ was smaller than $\mathrm{PCCMS}_{2, 3}$. Mode 1 had both small I_1 and MS_1; therefore, it gave the smallest $PCCMS_n$. Mode 6 had a smaller MS_6 than MS_1, but a much larger I_6 peaks than I_1 and even than other modes in general; thus, it gave a larger $PCCMS_6$ than $PCCMS_1$. Overall, at 10.15 GHz, mode 2 affected I the most. Based on Figure 13b and using the OSL algorithm, we can see that when the source is placed at x=137, the obtained I is probably the largest.

Figure 13c shows the obtained dependences of $|I|$ on x along the CSA length using CMA when the source was placed at the following positions: x=1 (the actual location of the feed), x=8, 26, 44, 66, 89, 112, 137, 169, 207, and 257 (the peak positions of the sum of $PCCMS_{1,2,3,5,6}$). By analyzing the results, we can say that when the source was placed at x=137, the $|I|$ was the largest, followed by 112, 207, 169, 257, 89, 8, 66, 26, 44, and 1. This is consistent with the prediction made by the OSL algorithm. The high $|I|$ obtained at 112, 207, 169, and 257 can be explained by the fact that when the source was excited at those segments, the sum of $PCCMS_{1,2,3,5,6}$ was high (except for x=129). Again, it can be noticed that $|I|$ for x=1 was the smallest, since I_n of all modes were very small at this segment (see Figure 13a). Note that at f=10.15 GHz, $|I|$ had the same shape as $|I_2|$.

In addition, when the source was placed at x=8 (near the edge of the CSA bottom surface), the obtained current was quite high compared to the currents for the x=66, 26, and 44 cases (unlike f=9.4 GHz, when the current at x=10 was only larger than that for x=55). This can be explained by the fact that when the source was placed at x=8, most of the modes were excited at their I_n peaks (see Figure 13a), and their sum of $PCCMS_n$ was larger than that for the x=66, 26, and 44 cases.

Figure 13d demonstrate that when the source was placed at x=137, the obtained E was the strongest, while at x=1, it was the weakest, which is consistent with all OSL predictions. In addition, despite the source position, the RP main lobes still had a similar direction (around 0°), which can be explained similarly to the case of f=9.4 GHz. It is worth noting that the RP back lobe level for x=8 is clearly larger than that for the other cases, followed by the x=26 case, which must be considered when it is important to control the antenna back radiation. Although x=1 was also located in the 1st loop, its current was much smaller than that of x=8. These observations were as follows: at 9.4 GHz, OSL was at x=129; and 10.15 GHz, OSL was at x=137.

For clarity, the characteristics of I and E when the source is placed at different positions and at various frequencies are presented in Table 2.

4. DISCUSSION

The proposed OSL algorithm provides a method to dynamically determine the OSL based on the operating frequency range and the structure itself. Although the newly developed algorithm has been applied only to dipoles and CSAs, this study demonstrated that it actually works. The proposed OSL algorithm has been validated by comparing the current and radiation field distribution results using CMA and MoM.

However, the verification of the obtained results with real measurements has not been done and will be done for more complex structures in the near future. The use of modes with MS greater than 0.1 as the modes with the largest influence on the current is based on the authors' experience. This value may be reduced when analyzing more complex structures, which means that the influence of more I_n on the surface current will be considered. In addition, as I_n increases, the implementation of the proposed algorithm becomes more complicated. Therefore, besides the fact that the use of OSL seems promising, it is also important to make it easier. In addition, the limitation of this algorithm is that it has not been applied yet to antennas that are excited by different feed types, especially if it is not directly connected to the antenna structure like in the case of exciting parabolic antennas, which is also a research aspect that needs to be considered in further studies.

Finding the source location should not only be limited to achieving the highest surface current. It should also be considered with respect to enhancing other useful antenna characteristics such as reflection coefficient, input impedance, etc. Moreover, further research should consider the feasibility of source location using the OSL algorithm to facilitate antenna installation according to the real situation. In addition, another important aspect that needs to be investigated is the efficiency of the proposed algorithm in more complicated requirements such as radiation at multiple frequencies or over a wide frequency range. In the future, it is possible to combine the OSL algorithm with the genetic algorithm to further optimize the antenna structure.

5. CONCLUSIONS

In this work, we have introduced an algorithm based on the analysis of eigenvalues and characteristic currents using CMA to determine the optimal source location that maximizes the surface current of complex WG structures. Beside the developed novel algorithm, the main contributions include demonstrating the effectiveness of the algorithm on the examples of two different structures, validating its accuracy by comparing the surface currents and the resulting radiation fields for various source positions, and verifying the results of the MATLAB code developed using CMA-based MoM with PBF by comparing its results with those obtained using conventional MoM with PBF. All this confirms the algorithm effectiveness in identifying the OSL for achieving the highest surface current across the frequency band. Moving forward, the developed algorithm and code hold promise for analyzing source placement in more complex WG antenna structures.

Acknowledgments

Funding: This research was funded by the Ministry of Science and Higher Education of the Russian Federation projects FEWM-2024-0005 and FEWM-2023-0014.

Conflicts of interest

The authors declare that they have no known competing financial interests or personal relationships that could have appeared to influence the work reported in this paper.

Authors contribution statement

Dang Tuan Phuong: Conceptualization, methodology, software, validation, formal analysis, data curation, writing—original draft preparation, visualization, project administration

Alhaj Hasan Adnan Faiezovich: Conceptualization, validation, formal analysis, writing—review and editing

Gazizov Talgat Rashitovich: Methodology, resources, writing—review and editing, supervision, funding acquisition

References

1. Tian, Q., Fan, H., Chen, J., et al. "Analysis and design of an airborne-dangled monopole-antenna symmetric remote-sensing radiation source for airport runway monitoring", *Symmetry*, **16**, p. 1069 (2024). https://doi.org/10.3390/sym16081069.

2. Keshwala, U., Ray, K., and Rawat, S. "Design and analysis of metamaterial integrated modified golden spiral antenna for terahertz applications", *Scientia Iranica*, **31**(14), pp. 1197–1205 (2024). https://doi.org/10.24200/sci.2022.58913.5963.

3. Ahmad, A., Zafrullah, M., and Ashraf, M. A., et al. "Art of antenna designing for 5G (mmWave) next generation networks", *2017 International Symposium on Wireless Systems and Networks (ISWSN)*, Lahore, Pakistan, pp. 1–4 (2017). https://doi.org/10.1109/ISWSN.2017.8250021.

4. Odiamenhi, M., Jahanbakhsh Basherlou, H., Hwang See, et al. "Advancements and challenges in antenna design and rectifying circuits for radio frequency energy harvesting", *Sensors*, **24**, p. 6804 (2024). https://doi.org/10.3390/s24216804.

5. Rawal, P. and Rawat, S. “A frequency and polarization reconfigurable L-shaped patch antenna with defected ground structure”, *Scientia Iranica*, **30**(5), pp. 1703–1713 (2023). https://doi.org/10.24200/sci.2021.57874.5451.
6. Çelik, K. “Highly miniaturized triple band classical patch shaped antenna for WLAN and WiMAX applications”, *Scientia Iranica* (2024). https://doi.org/10.24200/sci.2024.64204.8802.
7. Fedeli, A., Montecucco, and C., Gragnani, G.L. “Open-source software for electromagnetic scattering simulation: the case of antenna design”, *Electronics*, **8**, p. 1506 (2019). https://doi.org/10.3390/electronics8121506.
8. Deng X., Zhang D., Chen Y., et al. “Characteristic mode analysis: application to electromagnetic radiation, scattering, and coupling problems”, *Chinese Journal of Electronics*, **32**, pp. 663–677 (2023). https://doi.org/10.23919/cje.2022.00.200.
9. Sharma, I. B. Joshi, P., Shrimal, S., et al. “The design of multi band antenna with improved higher order mode radiation using CMA for L5-band, L1-band, and S-band application”, *Scientia Iranica*, (2024). https://doi.org/10.24200/sci.2023.62142.7669.
10. Harrington, R. and Mautz, J. “Theory of characteristic modes for conducting bodies”, *IEEE Transactions on Antennas and Propagation*, **19**(5), pp. 622–628 (1971). https://doi.org/10.1109/TAP.1971.1139999.
11. Russo, N.E., Zekios, C.L., and Georgakopoulos, S.V. “A CMA-based electronically reconfigurable dual-mode and dual-band antenna”, *Electronics*, **12**, p. 3915 (2023). https://doi.org/10.3390/electronics12183915.
12. Zhao, Y., Liang, L., Hu, Y., et al. “A Ka-Band silicon-based antenna-in-package design using characteristic mode analysis for bandwidth enhancement”, *Electronics*, **12**, p. 4983 (2023). https://doi.org/10.3390/electronics12244983.
13. Vu, D. T., Renaux, A., Boyer, R., et al. “Performance analysis of 2D and 3D antenna arrays for source localization”, *2010 18th European Signal Processing Conference*, Aalborg, Denmark, pp. 661–665 (2010). https://doi.org/10.5281/ZENODO.41886.
14. Belichenko, V.P., Buyanov, Y., Dymov, G, et al.. “Three-dimensional ultra-wideband antenna: from guiding physical considerations to sequential computer optimization of parameters and characteristics”, *Appl. Sci.*, **14**, 11658 (2024). https://doi.org/10.3390/app142411658.
15. Belichenko, V.P., Dymov, G.A., Tseplyaev, I.S, et al. “Rational approach to design of ultra-wideband printed antennas”, *Russ Phys J*, **66**, pp. 998–1004 (2023). https://doi.org/10.1007/s11182-023-03035-7.
16. Wang C. H., Chen Y. K., and Yang S. W. “Bandwidth enhancement of a dual-polarized slot antenna using characteristic modes”, *IEEE Antennas and Wireless Propagation Letters*, **17** (6), pp. 988–992 (2018). https://doi.org/10.1109/LAWP.2018.2828881.
17. Chen, Y. and Wang, C. F. “Characteristic-mode-based improvement of circularly polarized U-slot and E-shaped patch antennas”, *IEEE Antennas and Wireless Propagation Letters*, **11**, pp. 1474–1477 (2012). https://doi.org/10.1109/LAWP.2012.2231046.
18. Peitzmeier, N., Hahn, T., and Manteuffel, D. “Systematic design of multimode antennas for MIMO applications by leveraging symmetry,” *IEEE Transactions on Antennas and Propagation*, **70** (1), pp. 145–155 (2022). https://doi.org/ 10.1109/TAP.2021.3098610.
19. Li H., Sun S. N., Li W. C., et al., “Systematic pattern synthesis for single antennas using characteristic mode analysis,” *IEEE Transactions on Antennas and Propagation*, **68** (7), pp. 5199–5208 (2020). https://doi.org/10.1109/TAP.2020.2978939.
20. Yikai, C. and Chao, F. W. “Characteristic modes: theory and applications in antenna engineering”, Temasek Laboratories National University of Singapore. 284 p. (2015). https://doi.org/10.1002/9781119038900.
21. Hazdra, P. and Hamouz, P. “On the modal superposition lying under the MoM matrix equations”, *Radioengineering*, **17**(3) (2008). ISSN: 1210-2512, http://www.radioeng.cz/fulltexts/2008/08_03_042_046.pdf.
22. Alhaj Hasan, A., Nguyen, T.M., Kuksenko, S.P., et al. “Wire-grid and sparse MoM antennas: past evolution, present implementation, and future possibilities”, *Symmetry*, **15**, p. 378 (2023). https://doi.org/10.3390/sym15020378.
23. Nguyen M. T. “Innovative approaches to the design of sparse wire-grid antennas: development of algorithms and evaluation of their effectiveness,” *Systems of Control, Communication and Security*, (4), pp. 1–47 (2024). DOI: 10.24412/2410-9916-2024-4-001-047. URL: https://sccs.intelgr.com/archive/2024-04/01-Nguyen.pdf (in Russian).
24. Harrington, R. and Mautz, J. “Computation of characteristic modes for conducting bodies”, *IEEE Transactions on Antennas and Propagation*, **19**(5), pp. 629–639 (1971). https://doi.org/10.1109/TAP.1971.1139990.

25. Cabedo, F. M. “Systematic design of antennas using the theory of characteristic modes” Diss. Universitat Politècnica de València. 224p. (2008). ISBN: 978-91-7623-911-7, https://lup.lub.lu.se/search/publication/443cb111-f71b-49cb-b71f-ae59714e6cda.

26. Dang, T. P., Hasan, A. F. A., and Gazizov, T. R. “Analyzing the wire scatterer using the method of moments with the step basis functions”, *2024 Wave Electronics and its Application in Information and Telecommunication Systems (WECONF)*, St. Petersburg, Russian Federation, pp. 1–8 (2024). https://doi.org/10.1109/WECONF61770.2024.10564653.

27. Dang, T. P., Hasan, A. F. A., and Gazizov, T. R. “Performance comparison of correlation coefficient based trackers for characteristic mode analysis”, *2024 International Conference on Actual Problems of Electron Devices Engineering* (APEDE), Saratov, Russian Federation, pp. 102–106 (2024). https://doi.org/10.1109/APEDE59883.2024.10715817.

28. Hertel, T. W. and Smith, G. S. “The conical spiral antenna over the ground”, *IEEE Transactions on Antennas and Propagation*, **50**(12), pp. 1668–1675 (2002). https://doi.org/10.1109/TAP.2002.807429.

LIST OF CAPTIONS

Figure 1. Frequency dependences of MS_1 (black), MS_2 (red), and MS_3 (blue) obtained using CMA based on MoM with PBF (—) and CMA based on MoM with TBF (---) (MS – modal significance, CMA – characteristic mode analysis, MoM – method of moment, PBF – pulse basis function, TBF – triagular basis function)

Figure 2. The dependences of characteristic current I_n (*a*) and module of current $|I|$ (*b*) on number of segment x along the length of the dipole at frequency f=290 MHz. (CMA–characteristic mode analysis, MoM–method of moment)

Figure 3. The characteristic field E_n and radiation patterns (RPs) of the dipole at frequency f=290 MHz. (CMA–characteristic mode analysis, MoM–method of moment)

Figure 4. The dependences of characteristic current I_n (*a*) and module of current $|I|$ (*b*) on number of segment x along the length of the dipole at frequency f=520 MHz. (CMA–characteristic mode analysis, MoM–method of moment)

Figure 5. The characteristic field E_n and radiation patterns (RPs) of the dipole at frequency f=520 MHz. (CMA–characteristic mode analysis, MoM–method of moment)

Figure 6. The dependences of characteristic current I_n (*a*) and module of current $|I|$ (*b*) on number of segment x along the length of the dipole at frequency f=580 MHz. (CMA–characteristic mode analysis, MoM–method of moment)

Figure 7. The characteristic field E_n and radiation patterns (RPs) of the dipole at frequency f=580 MHz. (CMA–characteristic mode analysis, MoM–method of moment)

Figure 8. The dependences of characteristic current I_n (*a*) and module of current $|I|$ (*b*) on number of segment x along the length of the dipole at frequency f=800 MHz. (CMA–characteristic mode analysis, MoM–method of moment)

Figure 9. The characteristic field E_n and radiation patterns (RPs) of the dipole at frequency f=800 MHz. (CMA–characteristic mode analysis, MoM–method of moment)

Figure 10. The conical spiral antenna (CSA) isometric view (*a*) and the MATLAB CSA model (*b*).

Figure 11. The frequency dependences of MS_n for the conical spiral antenna CSA obtained using CMA based on MoM with PBF. (MS–modal significance, CMA – characteristic mode analysis, MoM – method of moment, PBF – pulse basis function)

Figure 12. The dependences of characteristic current I_n (*a*), $PCCMS_n$ (*b*), and module of current $|I|$ (*c*) on number of segment x and CSA RPs (*d*) at frequency f=9.4 GHz. (PCCMS – Product of Characteristic Current and Modal Significance, CMA – characteristic mode analysis, MoM – method of moment, CSA – conical spiral antenna, RP – radiation pattern)

Figure 13. The dependences of characteristic current I_n (*a*), $PCCMS_n$ (*b*), and module of current $|I|$ (*c*) on number of segment x and CSA RPs (*d*) at frequency f=10.15 GHz. (PCCMS – Product of Characteristic Current and Modal

Significance, CMA – characteristic mode analysis, MoM – method of moment, CSA – conical spiral antenna, RP – radiation pattern)

Table 1. Characteristics of module of current |*I*| and field *E* for the dipole antenna after OSL algorithm when the source is placed at different positions and at various frequencies (RP – radiation patterns)

Table 2. Characteristics of module of current |*I*| and field *E* for the CSA after the OSL algorithm when the source is placed at different positions and at various frequencies (PCCMS – Product of Characteristic Current and Modal Significance, RP – radiation patterns)

FIGURES

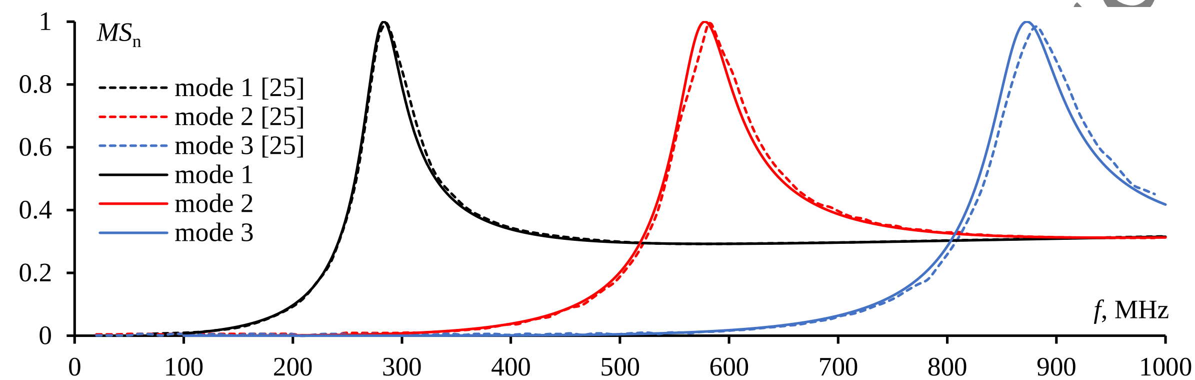

Figure 1.

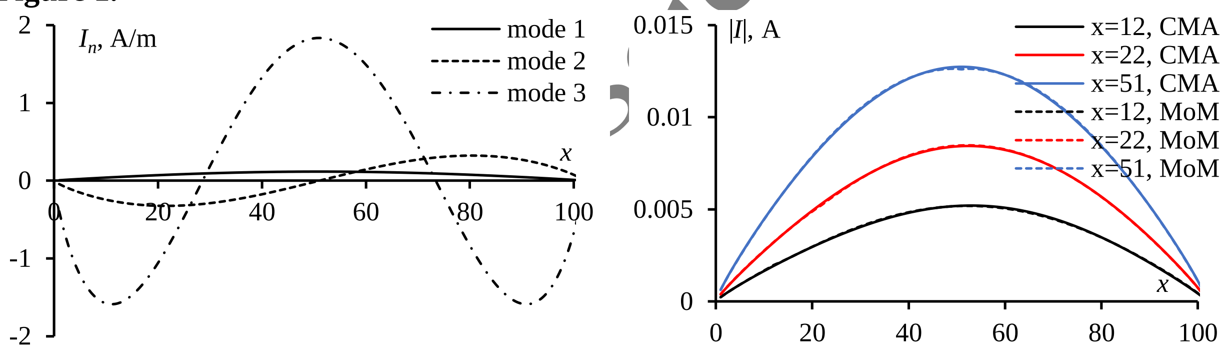

(a) (b)

Figure 2.

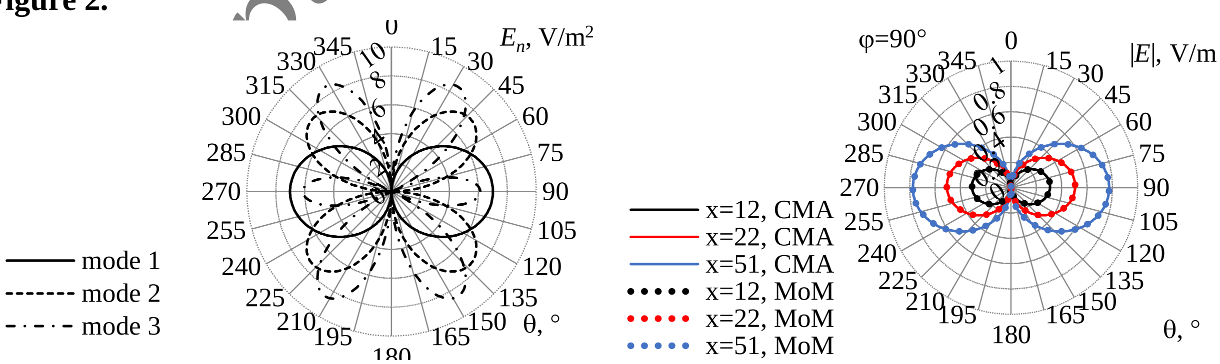

(a) (b)

Figure 3.

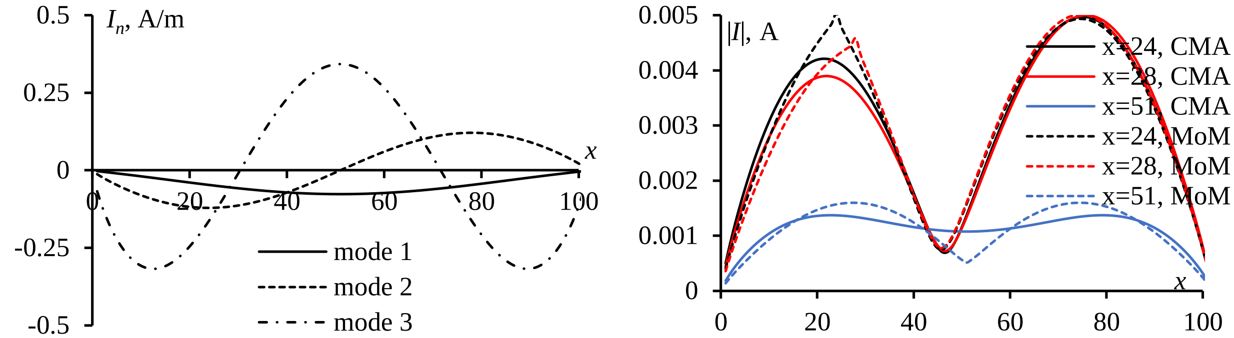

(a) (b)

Figure 4.

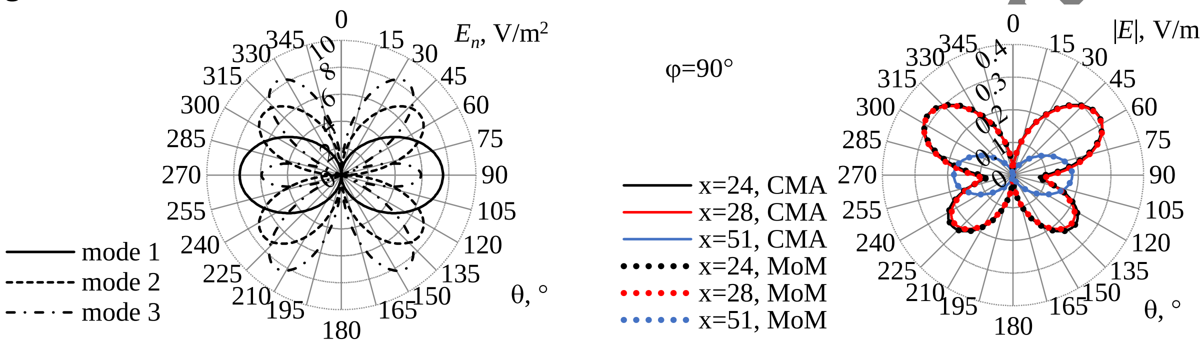

(a) (b)

Figure 5.

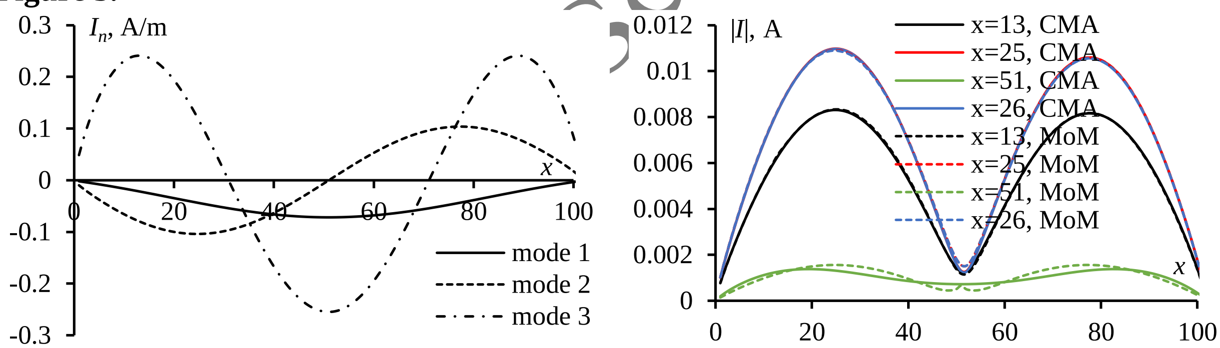

(a) (b)

Figure 6.

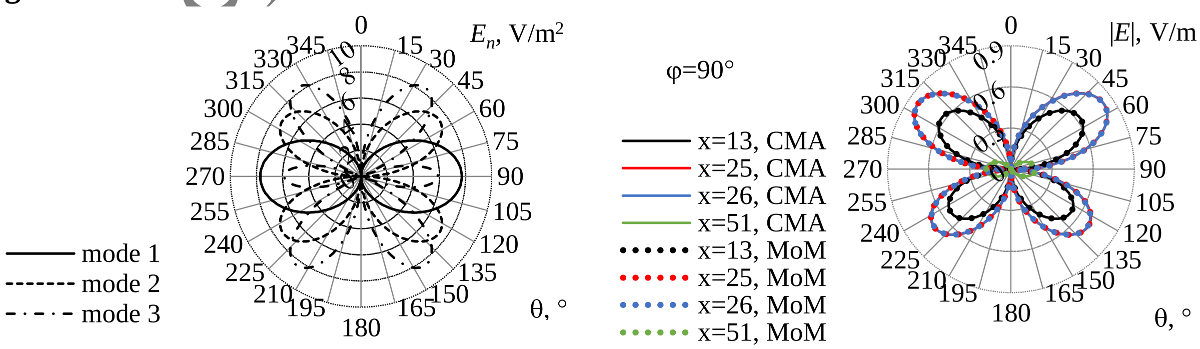

(a) (b)

Figure 7.

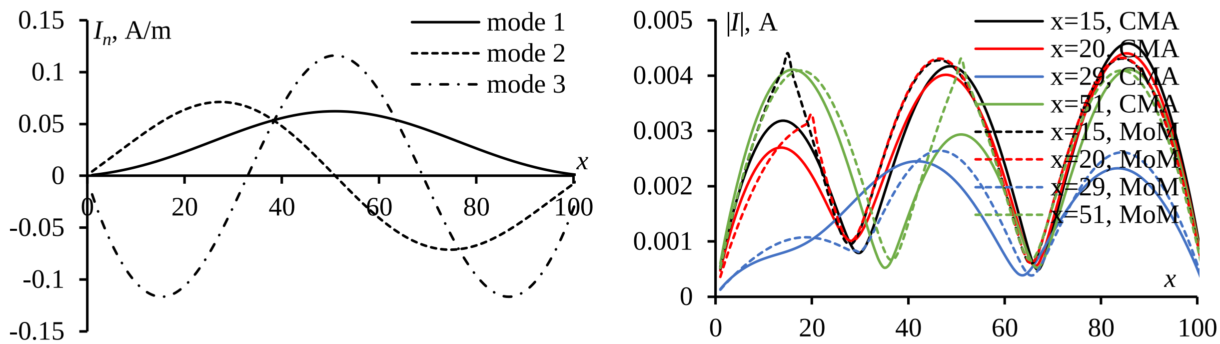

(a) (b)

Figure 8.

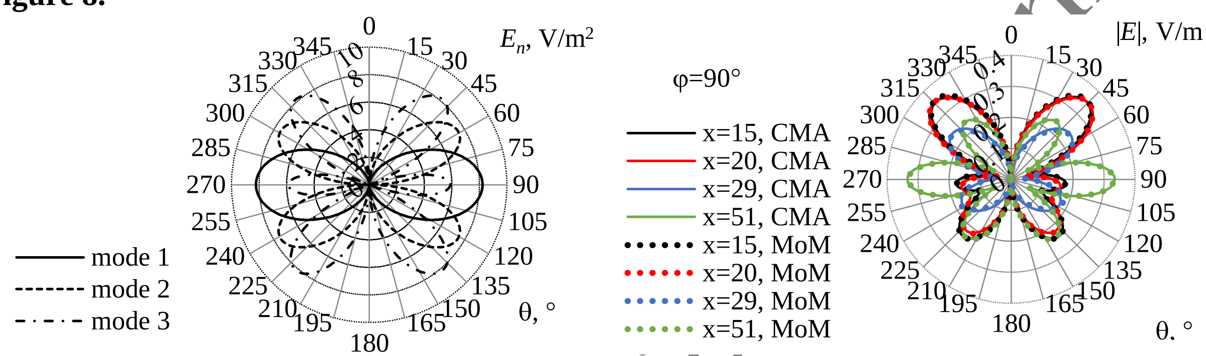

(a) (b)

Figure 9.

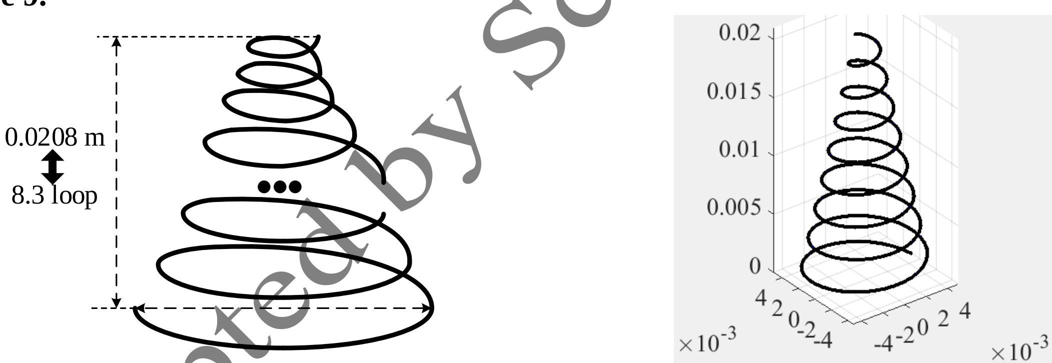

(a) (b)

Figure 10.

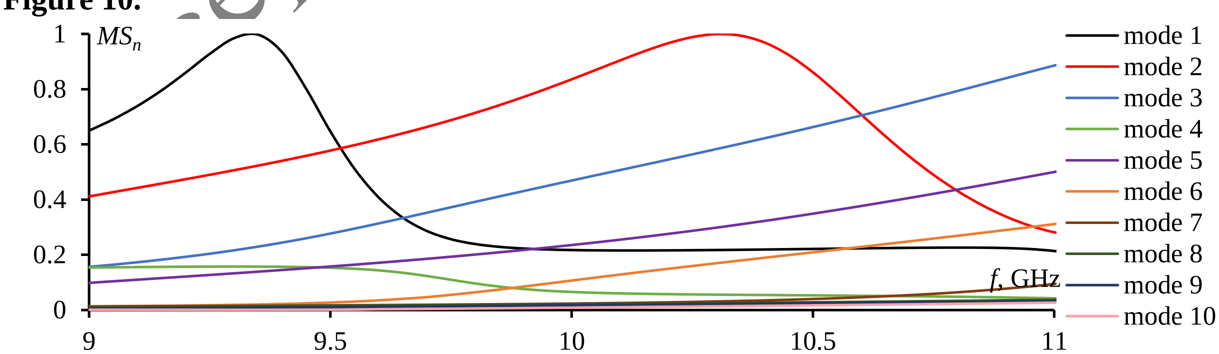

Figure 11.

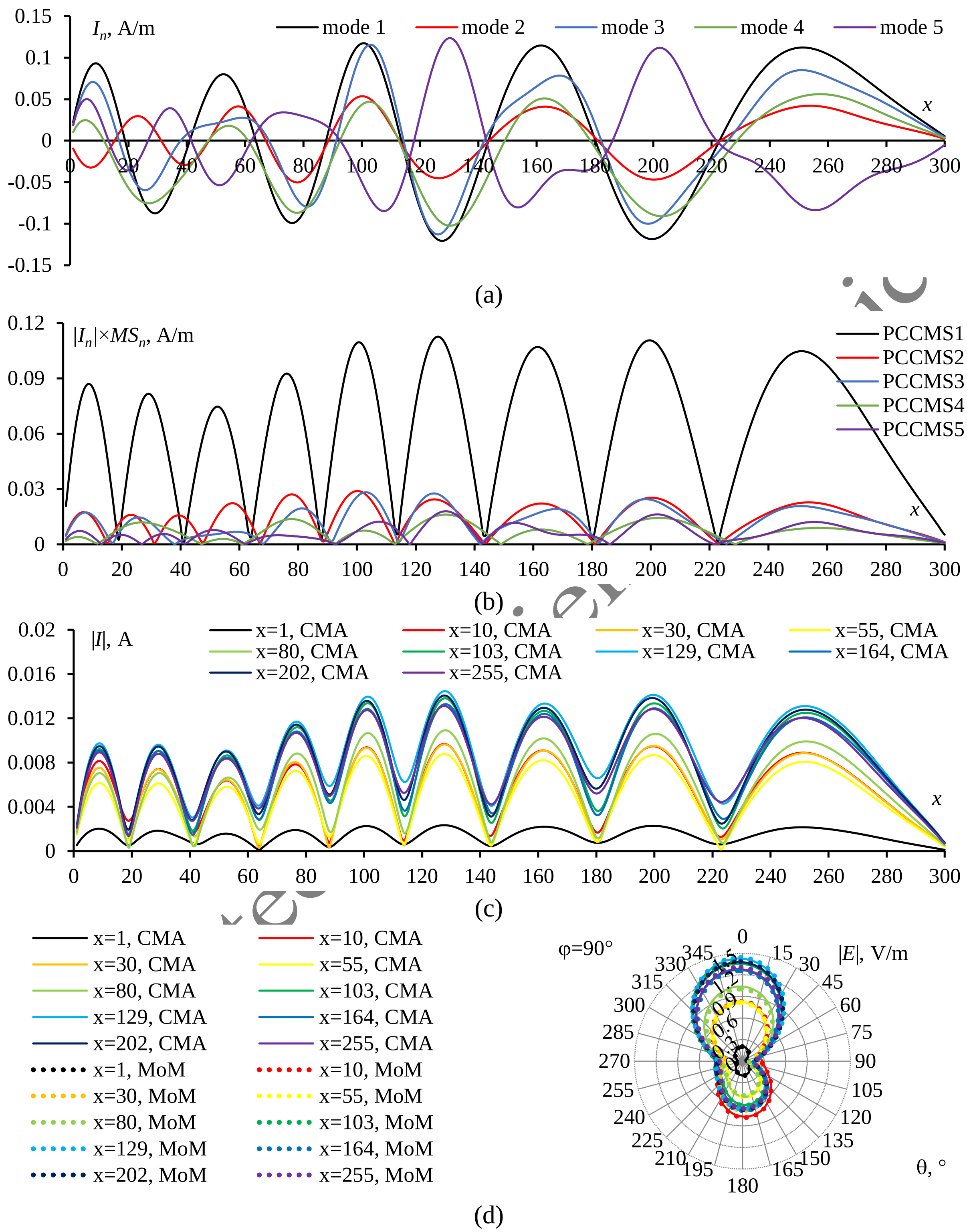

I_n, A/m
mode 1
mode 2
mode 3
mode 4
mode 5
0.15
0.1
0.05
0
-0.05
-0.1
-0.15
0 20 40 60 80 100 120 140 160 180 200 220 240 260 280 300
x
(a)
$|I_n|\times MS_n$, A/m
PCCMS1
PCCMS2
PCCMS3
PCCMS4
PCCMS5
0.12
0.09
0.06
0.03
0
0 20 40 60 80 100 120 140 160 180 200 220 240 260 280 300
x
(b)
|I|, A
x=1, CMA
x=10, CMA
x=30, CMA
x=55, CMA
x=80, CMA
x=103, CMA
x=129, CMA
x=164, CMA
x=202, CMA
x=255, CMA
0.02
0.016
0.012
0.008
0.004
0
0 20 40 60 80 100 120 140 160 180 200 220 240 260 280 300
x
(c)
x=1, CMA
x=10, CMA
x=30, CMA
x=55, CMA
x=80, CMA
x=103, CMA
x=129, CMA
x=164, CMA
x=202, CMA
x=255, CMA
x=1, MoM
x=10, MoM
x=30, MoM
x=55, MoM
x=80, MoM
x=103, MoM
x=129, MoM
x=164, MoM
x=202, MoM
x=255, MoM
φ=90°
|E|, V/m
θ, °
0 15 30 45 60 75 90 105 120 135 150 165 180 195 210 225 240 255 270 285 300 315 330 345
(d)

Figure 12.

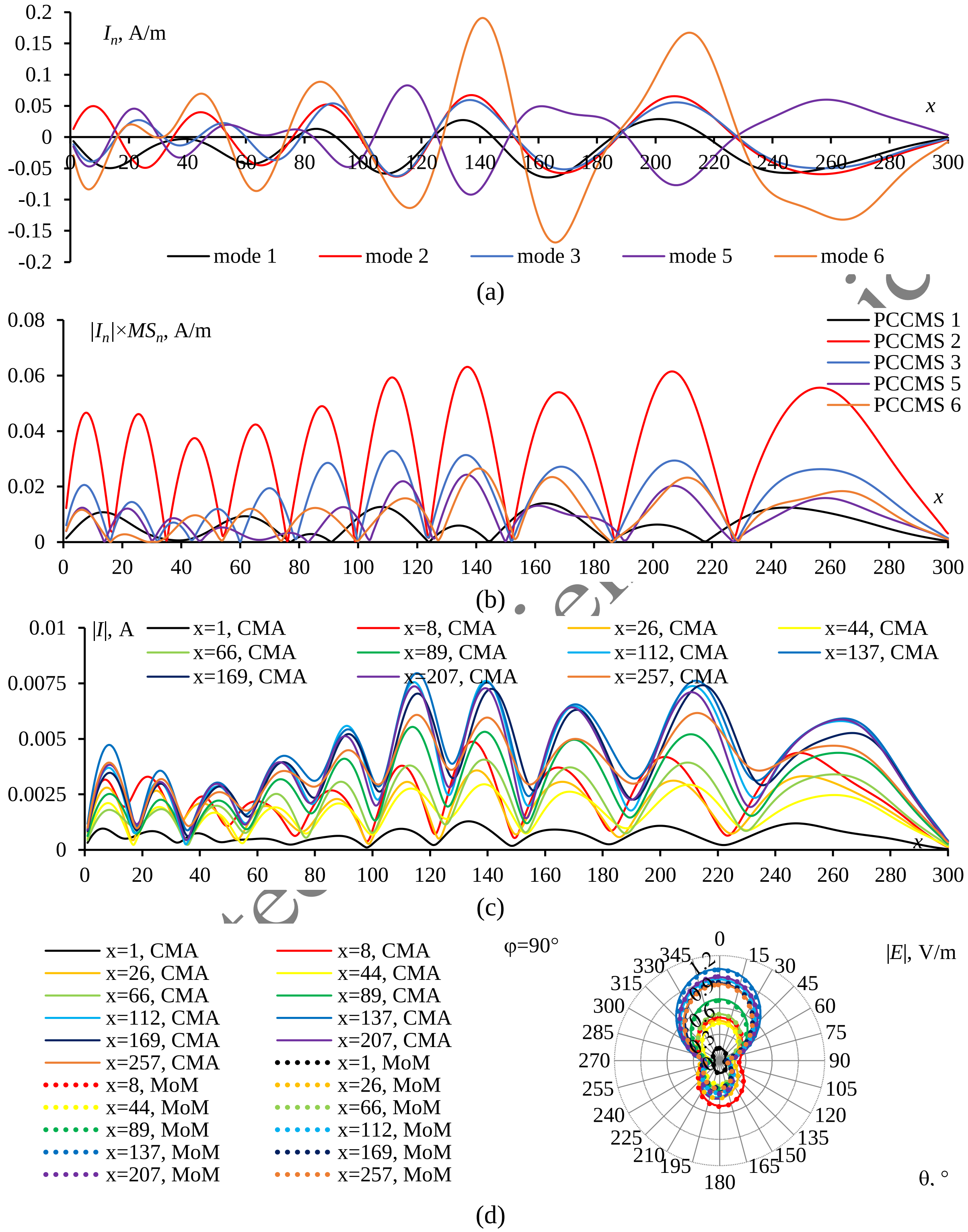

I_n, A/m
mode 1
mode 2
mode 3
mode 5
mode 6
(a)
$|I_n|\times MS_n$, A/m
PCCMS 1
PCCMS 2
PCCMS 3
PCCMS 5
PCCMS 6
(b)
$|I|$, A
x=1, CMA
x=8, CMA
x=26, CMA
x=44, CMA
x=66, CMA
x=89, CMA
x=112, CMA
x=137, CMA
x=169, CMA
x=207, CMA
x=257, CMA
(c)
x=1, MoM
x=8, MoM
x=26, MoM
x=44, MoM
x=66, MoM
x=89, MoM
x=112, MoM
x=137, MoM
x=169, MoM
x=207, MoM
x=257, MoM
φ=90°
$|E|$, V/m
θ, °
(d)

Figure 13.

TABLES

Table 1.

f, MHz	*x*	$\lvert I\rvert_{max}$, A	RP upper lobe		RP back lobe	
			$\lvert E\rvert_{max}$, V/m	θ, °	$\lvert E\rvert_{max}$, V/m	θ, °
290	**51**	**0.0127**	**0.77**	**90**	**0.77**	**90**
	22	0.0085	0.5	90	0.5	90
	12	0.0052	0.31	90	0.31	90
520	**28**	**0.005**	**0.32**	**56**	**0.226**	**129**
	24	0.005	0.32	55	0.24	129
	51	*0.0015*	*0.18*	*90*	*0.18*	*90*
580	**26**	**0.011**	**0.82**	**55**	**0.7**	**127**
	25	0.011	0.82	55	0.7	127
	13	0.008	0.62	53	0.54	126
	51	*0.0014*	*0.18*	*90*	*0.18*	*90*
800	**15**	**0.0045**	**0.35**	**44**	**0.24**	**140**
	20	0.0043	0.35	45	0.22	138
	51	*0.004*	*0.334*	*90*	*0.236*	*142*
	29	0.0023	0.24	52	0.176	117
880	**18**	**0.0096**	**0.842**	**44**	**0.681**	**139**
	16	0.0096	0.844	44	0.699	139
	51	*0.009*	*0.774*	*43*	*0.497*	*90*
	30	0.004	0.358	47	0.155	144

Table 2.

f, GHz	*x*	$\sum PCCMS_n$ peak, A/m	$\lvert I\rvert_{max}$, A	RP upper lobe		RP back lobe	
				$\lvert E\rvert_{max}$, V/m	θ, °	$\lvert E\rvert_{max}$, V/m	θ, °
9.4	**129**	**0.194**	**0.0144**	**1.427**	**357**	**0.6752**	**175**
	202	0.187	0.014	1.378	357	0.677	175
	103	0.178	0.014	1.357	356	0.6101	173
	255	0.167	0.0131	1.281	356	0.649	175
	164	0.16	0.0133	1.271	356	0.697	175
	80	0.143	0.011	1.039	357	0.497	174
	10	0.121	0.0097	0.824	358	0.77	175
	30	0.111	0.0097	0.828	356	0.683	177
	55	0.106	0.0088	0.83	356	0.507	173
	1	0.035	0.0023	0.2	0	0.2	175
10.15	**137**	**0.1422**	**0.0079**	**1.046**	**359**	**0.438**	**187**
	112	0.126	0.0076	0.93	359	0.421	186
	207	0.132	0.0073	0.954	359	0.436	188
	169	0.115	0.0074	0.88	0	0.359	185
	257	0.114	0.0062	0.873	359	0.3677	186
	89	0.096	0.0055	0.699	0	0.352	187

f, GHz	*x*	∑*PCCMS*$_n$ peak, A/m	$\|I\|_{max}$, A	RP upper lobe		RP back lobe	
				$\|E\|_{max}$, V/m	θ, °	$\|E\|_{max}$, V/m	θ, °
	8	0.089	0.0049	0.49	1	0.519	177
	66	0.069	0.0041	0.531	0	0.319	189
	26	0.068	0.0036	0.458	355	0.429	185
	44	0.051	0.0029	0.425	2	0.29	184
	1	0.026	0.00128	0.142	357	0.142	177

Dang Tuan Phuong received the specialist degree in special radio engineering systems from Yaroslavl Higher Military School of Anti-Aircraft Warfare, Yaroslavl, Russia, in 2023. He is currently pursuing the Ph.D. degree in electromagnetic compatibility of radio electronic devices (TUSUR). His current research interests include software and numerical methods for simulating electromagnetic scattering structures, especially sparse scatterer.

Alhaj Hasan Adnan Faiezovich received B.S. degree in information and communication technologies from the University of Tartous, Syria, in 2016, and M.S. degree in radio engineering from TSTU, Tambov, Russia, in 2019, and Ph.D. degree in radio engineering from TUSUR, Tomsk, Russia, in 2023. He has over five years of experience with electromagnetic compatibility and antennas problems. He has authored or coauthored over 150 refereed publications. His current research interests include electromagnetic compatibility, high-speed interconnects, antennas computer modeling, and numerical methods.

Gazizov Talgat Rashitovich received an Engineering degree, a Ph.D. degree, and a D.Sc. degree from TUSUR, Tomsk, Russia, in 1985, 1999, and 2010, respectively. He has authored or coauthored over 500 refereed publications, including 11 books. His current research interests include electromagnetic compatibility, numerical methods, high-speed interconnects, antennas computer modeling.